Zeeman splitting and dynamical mass generation in Dirac semimetal ZrTe$_5$

Yanwen Liu[1,2,3], Xiang Yuan[1,2,3], Cheng Zhang[1,2,3], Zhao Jin[4], Awadhesh Narayan[5,6], Chen Luo[7], Zhigang Chen[8], Lei Yang[8], Jin Zou[8,9], Xing Wu[7], Stefano Sanvito[5], Zhengcai Xia[4], Liang Li[4], Zhong Wang[10,11] & Faxian Xiu[1,2,3]

Dirac semimetals have attracted extensive attentions in recent years. It has been theoretically suggested that many-body interactions may drive exotic phase transitions, spontaneously generating a Dirac mass for the nominally massless Dirac electrons. So far, signature of interaction-driven transition has been lacking. In this work, we report high-magnetic-field transport measurements of the Dirac semimetal candidate ZrTe$_5$. Owing to the large g factor in ZrTe$_5$, the Zeeman splitting can be observed at magnetic field as low as 3 T. Most prominently, high pulsed magnetic field up to 60 T drives the system into the ultra-quantum limit, where we observe abrupt changes in the magnetoresistance, indicating field-induced phase transitions. This is interpreted as an interaction-induced spontaneous mass generation of the Dirac fermions, which bears resemblance to the dynamical mass generation of nucleons in high-energy physics. Our work establishes Dirac semimetals as ideal platforms for investigating emerging correlation effects in topological matters.

[1] State Key Laboratory of Surface Physics, Fudan University, Shanghai 200433, China. [2] Department of Physics, Fudan University, Shanghai 200433, China. [3] Collaborative Innovation Center of Advanced Microstructures, Nanjing 210093, China. [4] Wuhan National High Magnetic Field Center, Huazhong University of Science and Technology, Wuhan 430074, China. [5] School of Physics, AMBER and CRANN Institute, Trinity College, Dublin 2, Ireland. [6] Department of Physics, University of Illinois at Urbana—Champaign, Urbana, Illinois 61801, USA. [7] Shanghai Key Laboratory of Multidimensional Information Processing, Department of Electrical Engineering, East China Normal University, Shanghai 200241, China. [8] Materials Engineering, The University of Queensland, Brisbane, Queensland 4072, Australia. [9] Centre for Microscopy and Microanalysis, The University of Queensland, Brisbane, Queensland 4072, Australia. [10] Institute for Advanced Study, Tsinghua University, Beijing 100084, China. [11] Collaborative Innovation Center of Quantum Matter, Beijing 100871, China. Correspondence and requests for materials should be addressed to F.X. (email: faxian@fudan.edu.cn).

In the past few decades, transition-metal pentatelluride $ZrTe_5$ has attracted considerable attentions for its mysterious temperature anomaly[1,2]. Charge density wave was believed to be the origin of the anomalous peak in the temperature-dependent resistance but later it was excluded by experiments[2]. At the same time, both theory[3] and experiments[4–6] demonstrated that the band structure of $ZrTe_5$ is very complicated with multiple bands contributing to the electronic properties. Both single-frequency[5,6] and multi-frequency[4] Shubnikov–de Haas (SdH) oscillations were reported in $ZrTe_5$, suggesting a strong dependency of the electron states on the Fermi energy, E_F, in the band structure.

Recently, this material was reinvestigated as a candidate of Dirac semimetal[7]. A linear energy–momentum dispersion of the electronic structure in $ZrTe_5$ was demonstrated by angle-resolved photoemission spectroscopy (ARPES)[8] and optical spectroscopy measurements[9,10]. The negative magnetoresistance caused by chiral magnetic effect was also observed through magneto-transport[8]. These experimental evidences all suggest that $ZrTe_5$ is a Dirac semimetal candidate, which is similar to other Dirac semimetals[11–16] with extremely large magnetoresistance[17–19] and the negative magnetoresistance[8,20–22] possibly induced by the chiral anomaly. Although the single-particle physics of Dirac semimetals, including $ZrTe_5$ is under intense study, the many-body correlation effects are much less investigated. A high magnetic field would significantly enhance the density of states near the Fermi level, thus effectively amplifying the correlation effects. It is therefore highly desirable to investigate the behaviour of $ZrTe_5$ in the high-magnetic field regime. Possible phase transitions in high-magnetic fields have been reported in semimetallic graphite and bismuth[23–29], which, however, are not ideal Dirac semimetals. For Dirac and Weyl semimetals, it has been theoretically suggested that a high-magnetic field may induce the dynamical mass generation[30–34], namely, a Dirac mass is spontaneously generated by interaction effects. Depending on material details, the Dirac mass can manifest itself as charge density wave[30,33,35], spin density wave[31] or nematic state[34]. Although the mass generation has been observed at the surface of two-dimensional (2D) topological crystalline insulators[36,37], so far there is no clear evidence of its occurrence in three-dimensional bulk Dirac materials, despite its closer resemblance to that occurring in particle physics[38]. Moreover, dynamical mass generation in three-dimensional Dirac semimetals hosts a number of unusual phenomena absent in two dimensions, for instance, it is expected that the topological dislocations associated with the dynamically generated mass may possess chiral modes[35,39,40], holding promises to dissipationless transport inside three-dimensional bulk materials.

Here we report systematic transport measurements of single-crystal $ZrTe_5$ under extremely large magnetic field. Our samples show good crystalline quality and exhibit sufficiently high electron mobility at low temperatures, enabling the observation of SdH oscillations under a relatively small magnetic field. By tilting the field direction, we mapped the morphology of the detected Fermi surface and examined the topological property of $ZrTe_5$. The extracted band parameters suggest $ZrTe_5$ to be a highly anisotropic material. Remarkably, with a weak magnetic field the spin degeneracy is lifted, generating a pronounced Zeeman splitting. Furthermore, by taking advantage of the tiny Fermi surface, this material can be driven into its quantum limit regime within 20 T, where all the carriers are confined in the lowest Landau level. Under the magnetic field, we observe sharp peaks in the resistivity, which are naturally explained as dynamical mass generation coming from Fermi surface nesting. The generated Dirac mass endows an energy gap to the nominally massless Dirac electrons, causing sharp increase in the resistivity.

These findings not only suggest $ZrTe_5$ a versatile platform for searching novel correlated states in Dirac semimetal but also show the possibility on field-controlled novel symmetry-breaking phases manifesting the Dirac mass in the study of Dirac and Weyl semimetals.

Results

Growth and hall-effect measurements. $ZrTe_5$ single crystals were grown by chemical vapour transport with iodine as reported elsewhere[41]. The bulk $ZrTe_5$ has an orthorhombic layered structure with the lattice parameters of $a = 0.38$ nm, $b = 1.43$ nm, $c = 1.37$ nm and a space group of $Cmcm$ (D_{2h}^{17})[7]. The $ZrTe_5$ layers stack along the b axis. In the a–c plane, $ZrTe_3$ chains along a axis are connected by Te atoms in the c axis direction. Figure 1a is a typical high-resolution transmission electron microscopy (HRTEM) image taken from an as-grown layered sample, from which the high crystalline quality can be demonstrated. The inset selected area electron diffraction pattern together with the HRTEM image confirms that the layer normal is along the b axis.

The temperature dependence of the resistance R_{xx} and Hall effect measurements provide information on the electronic states of a material in a succinct way. We first carried out regular transport measurements to extract the fundamental band parameters of as-grown $ZrTe_5$ crystals. In a Hall bar sample, the current was applied along the a axis and the magnetic field was applied along the b axis (the stacking direction of the $ZrTe_5$ layers). Figure 1b shows the temperature dependence of the resistance R_{xx} of $ZrTe_5$ under the zero field. An anomalous peak, the unambiguous hallmark of $ZrTe_5$ (ref. 4), emerges at around 138 K and is ascribed to the temperature-dependent Fermi energy shift of the electronic band structure[42]. The Hall effect measurements provide more information on the charge carriers responsible for the transport. The Hall coefficient changes sign around the anomaly temperature, implying the dominant charge carriers changing from holes to electrons (Fig. 1c). The nonlinear Hall signal suggests a multi-carrier transport at both low and high temperatures, which is also confirmed by the Kohler's plot and our first-principles electronic structure calculations (Supplementary Note 1 and Supplementary Figs 1–5). For convenience, a two-carrier transport model[43,44] is adopted to estimate the carrier density and mobility. The dominant electron exhibits an ultrahigh mobility of around 50,000 $cm^2 V^{-1} s^{-1}$ at low temperature, which leads to strong SdH oscillations as we will discuss later. Around the temperature of the resistance anomaly, the electron carrier density has already decayed to almost one-tenth of that at low temperature, and finally holes become the majority carriers at $T > 138$ K (Fig. 1d). Detailed analysis of the two-carrier transport is described in Supplementary Notes 1 and 2 and in Supplementary Figs 1–8.

Fermi surface and quantum oscillations analysis. Elaborate measurements of angle-dependent magnetoresistance (MR) provide further insight into the band-topological properties of $ZrTe_5$. A different external magnetic field geometry has been exploited to detect the Fermi surface at 2 K, as shown in Fig. 2. When the magnetic field $B > 0.5$ T is applied along the b axis, clear quantum oscillations can be identified, indicating a high mobility exceeding 20,000 $cm^2 V^{-1} s^{-1}$. The MR ratio $\frac{R(B) - R(0)}{R(0)}$ is around 10 (here $R(B)$ is the resistance under magnetic field B and $R(0)$ is the resistance under zero field), lower than previous results[8] on account of different Fermi level positions. As the magnetic field is tilted away from the b axis, the MR damps with the law of cosines, suggesting a quasi-2D nature and a highly anisotropic Fermi surface with the cigar/ellipsoid shape. This is reasonable for a
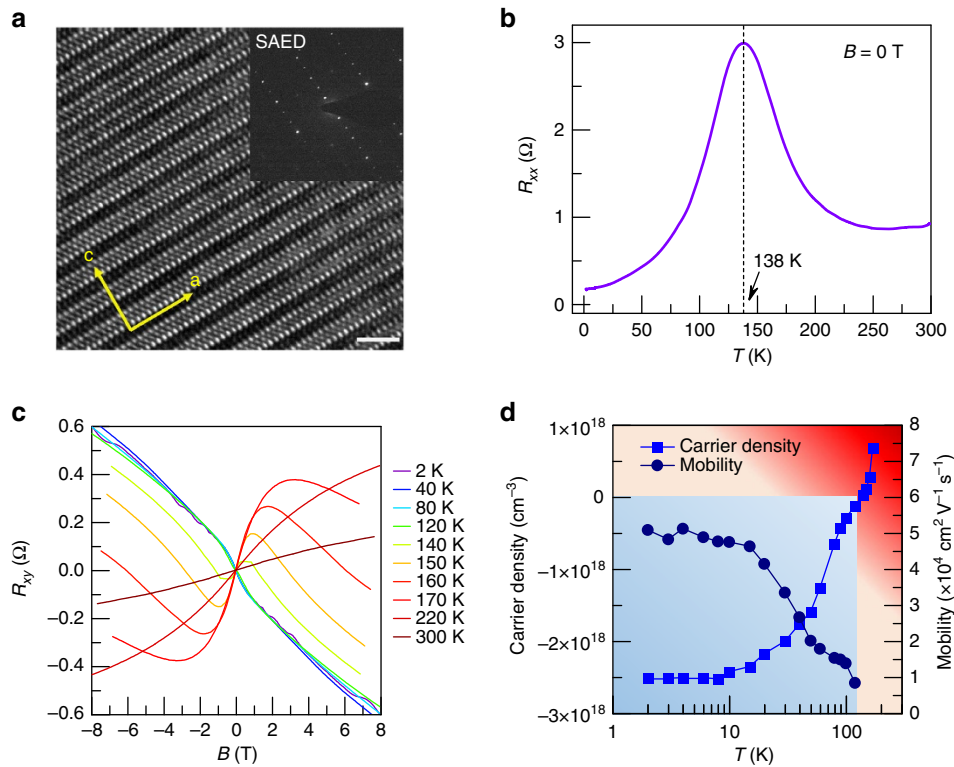
Figure 1 | Crystal structure and Hall effect measurements of ZrTe$_5$. (**a**) An HRTEM image of ZrTe$_5$ with an inset selected area electron diffraction (SAED) pattern, showing the layer normal along the b axis. The white scale bar corresponds to 2 nm. (**b**) Temperature-dependent resistance under zero magnetic field. An anomalous resistance peak occurs at $T \sim 138$ K. (**c**) Temperature-dependent Hall resistance of ZrTe$_5$. The nonlinear Hall slopes at both low temperature and high temperature demonstrate the multi-carrier transport in ZrTe$_5$. (**d**) The temperature-dependent mobility and carrier density of the dominant carriers. A transition of electron- to hole-dominated transport is observed around the temperature of the anomalous resistance peak. The graduated background represents the amount and type of carriers, blue for holes and red for electrons.

layered material[45]. A Landau fan diagram of arbitrary angle (Fig. 2b) is plotted to extract the oscillation frequency S_F and Berry's phase Φ_B according to the Lifshitz–Onsager quantization rule[46]: $\frac{S_F}{B} = N + \frac{1}{2} - \frac{\Phi_B}{2\pi} - \delta = N + \gamma$, where N is the Landau level index, S_F is obtained from the slope of Landau fan diagram and γ is the intercept. For Dirac fermions, a value of $|\gamma|$ between 0 and 1/8 implies a non-trivial π Berry's phase[46], whereas a value of around 0.5 represents a trivial Berry's phase. Here the integer indices denote the ΔR_{xx} peak positions in $1/B$, while half integer indices represent the ΔR_{xx} valley positions. To avoid the influence from the Zeeman effect, here we only consider the $N \geq 3$ Landau levels. With the magnetic field along the b axis, the Landau fan diagram yields an intercept γ of 0.14 ± 0.05, exhibiting a non-trivial Berry's phase for the detected Fermi surface. At the same time, S_F shows a small value of 4.8 T, corresponding to a tiny Fermi area of $4.6 \times 10^{-4}\,\text{Å}^{-2}$. The system remains in the non-trivial Berry's phase as long as $0 \leq \beta \leq 70°$ (Fig. 2b inset and Fig. 2c). We have also obtained the angular dependence of S_F as illustrated in the inset of Fig. 2c where a good agreement with a $1/\cos\beta$ relationship is reached, confirming a quasi-2D Fermi surface. However, as the magnetic field is rotated towards the c axis ($\beta > 70°$), the Berry's phase begins to deviate from the non-trivial and finally turns to be trivial when B is along the c axis (Fig. 2b inset, the two dark-red curves with intercept of ~ 0.5). Meanwhile, the oscillation frequency S_F deviates from the cosines law and gives a value of 29.4 T along the c axis (Fig. 2c inset). The Berry's phase development along with the angular-dependent S_F unveils the quasi-2D Dirac nature of ZrTe$_5$ and possibly a nonlinear energy dispersion along the c axis. This is also confirmed by the band parameters such as the effective mass and the Fermi velocity, as described below.

A meticulous analysis of the oscillation amplitude at different angles was conducted to reveal the electronic band structure of ZrTe$_5$. Following the Lifshitz–Kosevich formula[46–48], the oscillation component ΔR_{xx} could be described by

$$\Delta R_{xx} \propto R_T R_D R_S \cos 2\pi\left(\frac{S_F}{B} + \gamma\right), \quad (1)$$

where R_T, R_D and R_S are three reduction factors accounting for the phase smearing effect of temperature, scattering and spin splitting, respectively. Temperature-dependent oscillation ΔR_{xx} could be captured by the temperature smearing factor $R_T \propto \frac{2\pi^2 k_B T m^* / \hbar eB}{\sinh(2\pi^2 k_B T m^* / \hbar eB)}$, where k_B is the Boltzmann's constant, $\hbar$ is the reduced Plank's constant and m^* is the in-plane average cyclotron effective mass. By performing the best fit of the thermal damping oscillation to the equation, the effective mass $m_{a-c}^\star$ (when the magnetic field is applied along the b axis, the Fermi surface in a–c plane is detected) is extracted to be $0.026m_e$, where m_e is the free electron mass (Fig. 2d). Such a small effective mass agrees well with the Dirac nature along this direction; and it is comparable to previously reported Dirac[18,49,50] or Weyl semimetals[19]. The corresponding Fermi velocity yields a value of $5.2 \times 10^5\,\text{m s}^{-1}$, which agrees with recent ARPES results[42]. A similar analysis gives a value of $m_{a-b}^\star = 0.16m_e$ and $m_{b-c}^\star = 0.26m_e$, respectively (Fig. 2e; also see Supplementary Note 3, Supplementary Figs 9–11 and Supplementary Table 1 for detailed information). Both $m_{a-b}^\star$ and $m_{b-c}^\star$ are larger than $m_{a-c}^\star$; this indicates a deviation from linear dispersion of these two surfaces considering the weak interlayer coupling[7], which is in agreement with our previous results[51] and the reported ARPES[8]. The carrier lifetime τ could be obtained from the Dingle
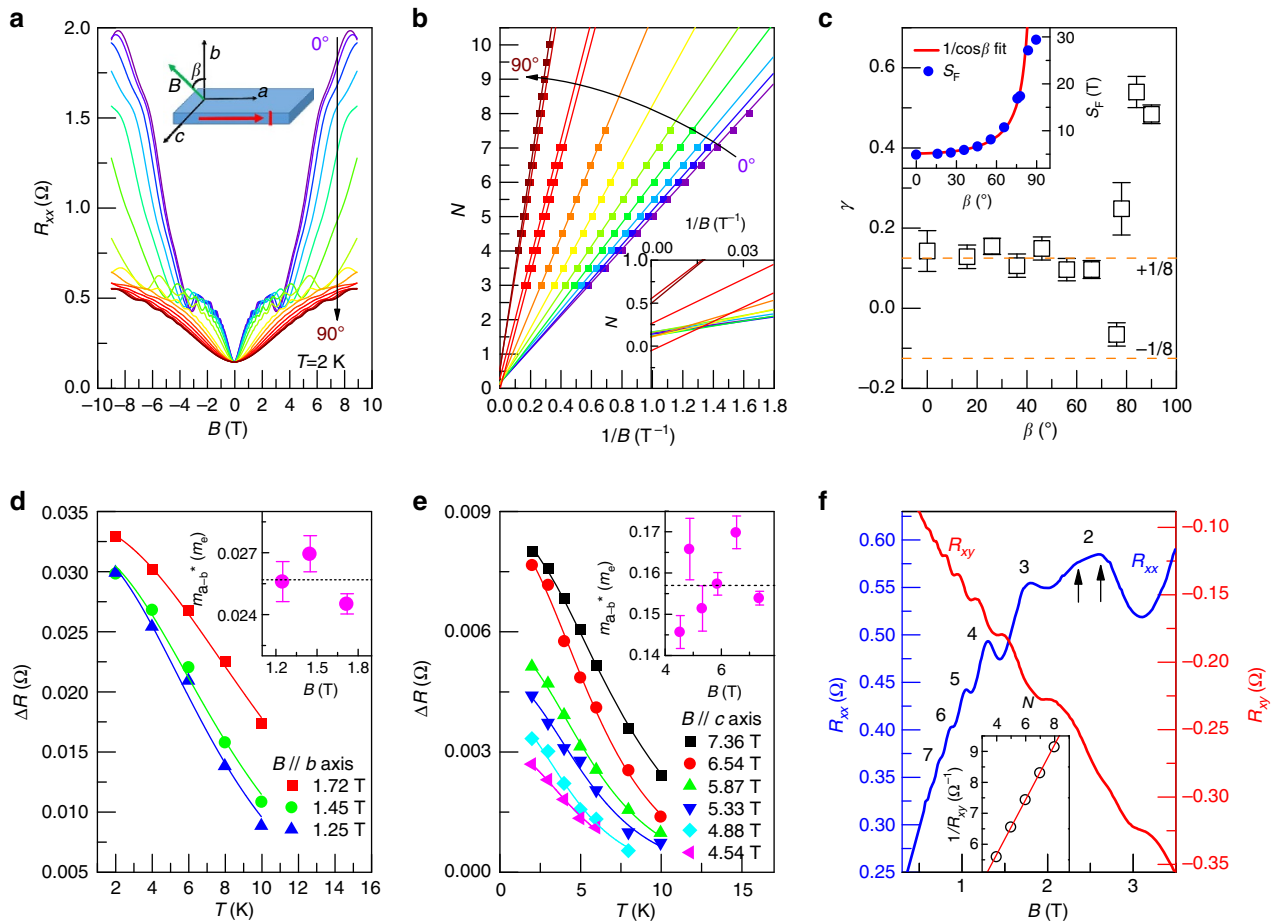
Figure 2 | Angular MR and SdH oscillations of ZrTe₅. (**a**) Angular MR of ZrTe$_5$. The inset shows the geometry of external magnetic field. (**b**) Landau fan diagram of arbitrary angle in **a**. Inset: Zoom-in view of the intercept on y axis. (**c**) The angular-dependent intercept of Landau fan diagram in **b**. Inset: angular-dependent oscillation frequency. The error bars were generated from the linear fitting process in the Landau fan diagrams. (**d,e**) The effective mass of ZrTe$_5$ when the magnetic field is applied along b axis and c axis, respectively. The error bars were generated from the fitting process. (**f**) The quantum oscillations of R_{xx} and quantized plateaus in R_{xy}.

Table 1 | Band parameters of ZrTe₅.

Geometry	Effective mass	Frequency	Fermi area	Fermi velocity	Lifetime
	$m^\star/m_e$	S_F (T)	A_F (Å^{-2})	v_F (10^5 ms^{-1})	τ (ps)
b–c plane	0.26	46.6	4.4×10^{-3}	1.7	0.16
a–c plane	0.026	4.8	4.6×10^{-4}	5.2	0.13
a–b plane	0.16	29.4	2.8×10^{-3}	2.2	0.21

The band parameters, including the effective mass m^*, Fermi surface S_F, Fermi area A_F, Fermi velocity v_F and lifetime τ can be extracted from the SdH oscillations.

factor $R_D \sim e^{-D}$, where $D = \frac{\pi m^*}{eB\tau}$. Table 1 summarizes the analysed parameters of the band structure.

Besides the obvious SdH oscillations of R_{xx}, R_{xy} exhibits distinct nearly quantized plateaus, whose positions show a good alignment with the valley of R_{xx} (Fig. 2f). The value of $1/R_{xy}$ establishes a strict linearity of the index plot and demonstrates the excellent quantization (Fig. 2f inset), reminiscent of the bulk quantum Hall effect. A similar behaviour has been observed in several highly anisotropic layered materials, such as the heavily n-doped Bi$_2$Se$_3$ (ref. 52), η-Mo$_4$O$_{11}$ (ref. 53) and organic Bechgaard salt[54–56]. At variance with the quantum Hall effect in a 2D electron gas, the quantization of the inverse Hall resistance does not strictly correspond to the quantum conductance. In fact, because of the weak interlayer interaction[7], bulk

ZrTe$_5$ behaves as a series of stacking parallel 2D electron channels with layered transport, which leads to the 2D-like magneto-transport as discussed above. The impurity or the coupling between the adjacent layers in the bulk causes the dissipation so that the R_{xx} cannot reach zero[52]. It is worth noting that the peak associated to the second Landau level in R_{xx} displays a broad feature with two small corners marked by the arrows, implying the emergence of spin splitting.

Zeeman splitting under extremely low temperature. It is quite remarkable that the spin degeneracy can be removed by such a weak magnetic field. To investigate the spin splitting, it is necessary to further reduce the system temperature. Figure 3a
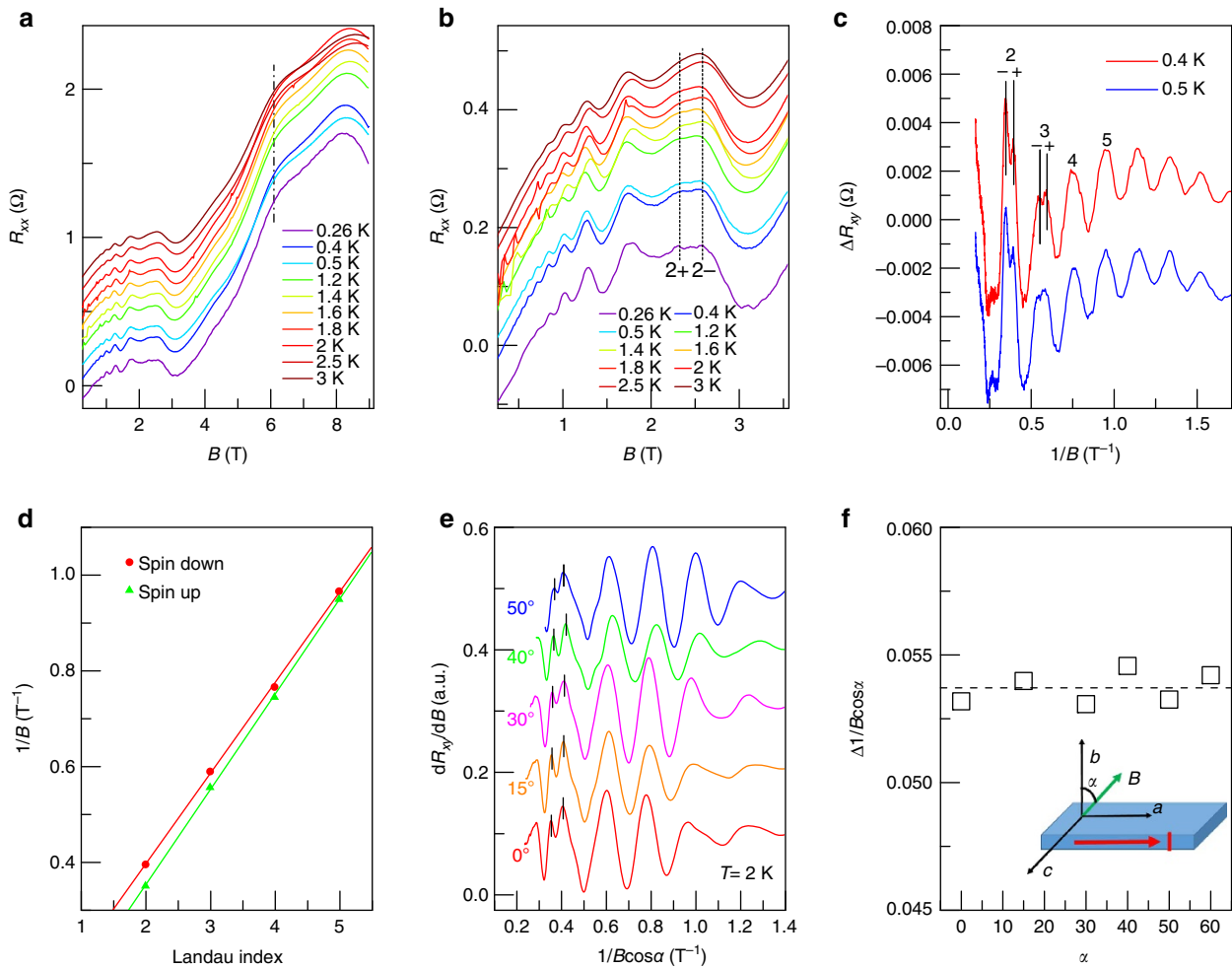
Figure 3 | Zeeman splitting in ZrTe₅. (**a**) MR behaviour of ZrTe$_5$ at the temperature range of 0.26–3 K. (**b**) Temperature-dependent MR of ZrTe$_5$. Two dashed lines are a guide to the eyes, which indicate the Zeeman splitting of the second Landau level. (**c**) The oscillation component in R_{xy} at 0.4 and 0.5 K. Sizable Zeeman splitting can be distinguished from the second and third Landau levels. (**d**) Landau fan diagram for both spin-up and spin-down electrons. (**e**) Angular dependence of the first-order differential R_{xy} versus $1/B\cos\alpha$. (**f**) The spacing of Zeeman splitting in the second Landau level at different field angles. The inset shows the geometry of external magnetic field.

shows the MR behaviour of ZrTe$_5$ at 260 mK. A peak deriving from the first Landau level can be observed at ~6 T. The second Landau level offers a better view of the Zeeman splitting because of the relatively small MR background, as marked by the dashed lines in Fig. 3b. The R_{xy} signal provides a much clearer signal: after subtracting the MR background, it reveals strong Zeeman splitting from the oscillatory component ΔR_{xy} (Fig. 3c and Supplementary Fig. 12). At 0.4 K, the fifth Landau level begins to exhibit a doublet structure with a broad feature. Under higher magnetic fields, the separation of the doublet structure increases, in particular, the second Landau level completely evolves into two peaks, indicating the complete lifting of spin degeneracy due to the Zeeman effect. To analyse the Zeeman effect occurred at such low temperature conveniently, we rearranged the spin phase factor $R_S = \cos\left(\frac{\pi g m^*}{2m_0}\right)$ in equation (1) by the product-to-sum formula[47] (detailed mathematical process is available in Supplementary Note 4). As a result, the oscillation component ΔR_{xx} is equivalent to the superposition of the oscillations from the spin-up and spin-down Fermi surface

$$\Delta R_{xx} \propto R_T R_D \left[\cos 2\pi \left(\frac{S_F}{B} + \gamma + \frac{1}{2}\varphi \right) + \cos 2\pi \left(\frac{S_F}{B} + \gamma - \frac{1}{2}\varphi \right) \right],$$
(2)

where $\varphi = \frac{g m^*}{2m_0}$ is the phase difference between the oscillations of spin-up and spin-down electrons. With this method we can estimate the g factor by Landau index plot for both spin ladders (Fig. 3d). This leads to the g factor of 21.3, in good agreement with the optical results[9]. Given such a large g factor, it is understandable that the Zeeman splitting could be easily observed in a relatively weak magnetic field. We have further carried out the theoretical Landau level calculations, which provides a clear insight into the Zeeman splitting as elaborated in Supplementary Note 5. In short, when the magnetic field is along the b axis (z direction), the Landau level energy eigenvalues for $n \neq 0$ are $E_n = \pm \sqrt{E_k^2 + \left(E_B\sqrt{n} \pm g\mu_B B/2\right)^2}$, where μ_B is the Bohr magneton, and in this case $E_k = \hbar v_z k_z$, $E_B = \sqrt{2\hbar v_x v_y eB}$ is the Landau level energy of the band bottom of the $n = 1$ Landau level. Here the Landau levels are split by $g\mu_B B$, resulting in the observed Zeeman splitting.

The angular-dependence of the Zeeman splitting can provide valuable information to probe the underlying splitting mechanism. Figure 3e shows the first-order differential R_{xy} as a function of $1/B\cos\alpha$. Pronounced quantum oscillations with Zeeman splitting can be unambiguously distinguished and they align well with the scale of $1/B\cos\alpha$, further verifying the quasi-2D Fermi surface as mentioned before. It is noticeable that the spacing of

the Zeeman splitting changes with the field angle. Generally, Zeeman splitting effect is believed to scale with the total external magnetic field so that the spacing of the splitting Landau level would not change with angle. However, in the case of ZrTe$_5$, the spacing of the Zeeman splitting, normalized by $B\cos\alpha$, is consistent with the quasi-2D nature (Fig. 3f). The angular dependent Zeeman splitting can be attributed to the orbital contribution caused by strong spin-orbit coupling in ZrTe$_5$ (ref. 7). Regarding the effect of the exchange interaction induced by an external field, we may decompose the splitting into an orbital-dependent and an orbital-independent part, where the former one depends on the shape of the band structure that leads to the angle-dependent splitting, and the latter one mainly comes from the Zeeman term that hardly contributes to any angular dependent splitting[11]. Owing to the highly anisotropic Fermi surface of ZrTe$_5$ and the strong spin orbital coupling from the heavy Zr and Te atoms, the orbital effect in the a–c plane of ZrTe$_5$ is significant, giving rise to a highly anisotropic g factor and an angular-dependent Zeeman splitting. Similar phenomena have also been observed in materials such as Cd$_3$As$_2$ (refs 49,57) and Bi$_2$Te$_3$ (ref. 58).

Magnetotransport under high magnetic fields. A high magnetic field up to 60 T was applied to drive the sample to the ultra-quantum limit to search for possible phase transitions. Figure 4a shows the angular-dependent MR of ZrTe$_5$ under strong magnetic field. The measurement geometry can be found in Fig. 3f inset. Several features are immediately prominent. First, when the

magnetic field is along the a axis, Zeeman splitting is observed, which is consistent with the theoretically solved Landau levels (Supplementary Note 5). The g factor along the a axis extracted by formula (2) is 3.19, which agrees well with the anisotropy of g factor discussed above (Supplementary Fig. 13). When the magnetic field is along the c axis, spin-splitting is hardly observed, again consistent with the theoretical expectations and the recent magneto-spectroscopy results[9] (Supplementary Note 6 and Supplementary Fig. 14). Here the Landau level energy eigenvalues become $E_n = \pm\sqrt{nE_B^2 + (E_k \pm g\mu_B B/2)^2}$, here $E_k = \hbar v_y k_y$. The effect of the magnetic field is the horizontal shifting of the degenerate Landau levels by $\pm g\mu_B B/\hbar v_y$ in the k_y vector direction (the field direction), instead of splitting the heights of the band bottom like the case when the field is along the a or b axis, thus there is no Landau level splitting in the quantum oscillation. Second, even with an external magnetic field up to 60 T (in the quantum limit regime), the MR feature still follows the $B\cos\alpha$ fitting, confirming once again the quasi-2D nature of ZrTe$_5$ (Fig. 4b). Finally, and most importantly, a huge resistance peak emerges at around 8 T, followed by a flat valley between 12 and 22 T, then the resistance increases and forms a shoulder-like peak at ~30 T. It should be emphasized that the amplitude of the resistance at 8 T is much larger than the amplitude of SdH oscillations, so that the signal of the first Landau level has been submerged into the anomalous peak. Only a few materials show analogous field-induced electronic instabilities, such as bismuth[23,24,26], graphite[25,29,59], and more recently the Weyl semimetal TaAs (ref. 60). As we have remarked,
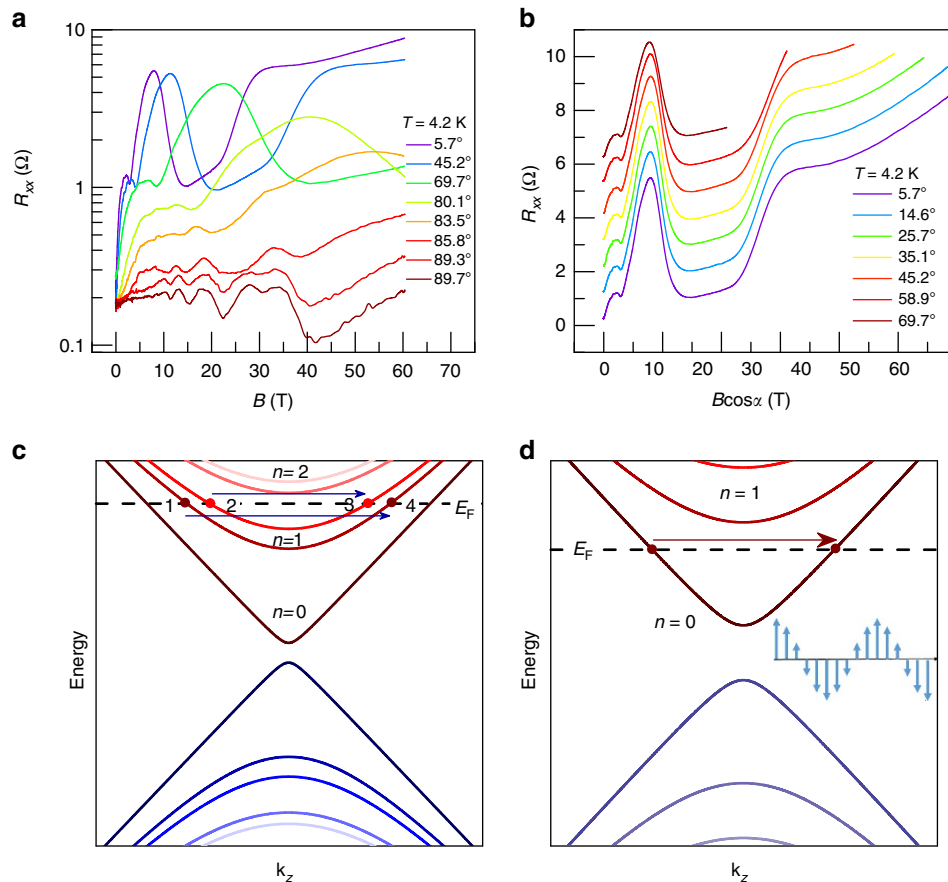

Figure 4 | Ultra-quantum limit transport and dynamical mass generation of ZrTe$_5$ at 4.2 K. (**a**) Angular-dependent MR of ZrTe$_5$ at 4.2 K under high magnetic field up to 60 T. (**b**) Angular-dependent MR as a function of effective magnetic field perpendicular to a–c plane. (**c,d**) The Landau levels and Fermi levels for $B \approx 9$ and 25 T, respectively. The inset of **d** is an illustration of the spin density wave from the $n=0$ Landau level.

the SdH peak due to the $n = 1$ Landau level merges into the anomalously large peak around $B = 8$ T, which suggests that the $n = 2$ Landau levels are empty and the electrons in the $n = 1$ Landau level are responsible for the anomalous peak. The location of Fermi level is schematically shown in Fig. 4c. The peak can be naturally explained by the picture of dynamical mass generation (accompanied by a density wave formation, with the wave vector being the nesting vector) in the $n = 1$ Landau levels, which leads to the generation of an energy gap for the electrons in these Landau levels, thus significantly enhancing the resistivity. In Fig. 4c, we illustrate one of the possibilities of nesting vectors responsible for this instability (the other possibility being two vectors connecting the Fermi momenta 1 to 3, and 2 to 4, respectively). Since the vector $\overrightarrow{23}$ is slightly different from the vector $\overrightarrow{14}$ due to the Zeeman splitting, the density wave transition should also be Zeeman split, which is presumably responsible for the existence of a 'bump' near the top of the peak in Fig. 2a.

On further increasing the magnetic field, the resistivity reaches a minimum at around $B = 14$ T (Fig. 4b), which can be explained as a reentrant transition due to the crossing of the Fermi level with the band bottom of the $n = 1$ Landau level. A similar phenomenon has been observed in graphite[61]. In fact, if we take a simple Bardeen–Cooper–Schrieffer model for the density wave state, we have $k_B T_c = 1.14(E_F - E_B) \exp\left(-\frac{1}{N(0)V}\right)$, which predicts that $T_c = 0$ as E_F approaches E_B, leading to the destruction of density waves. Here $N(0)$ and V are the density of states at the Fermi level and the interaction parameter (of the order of several eV), respectively. As the magnetic field increases, the density wave in the first Landau level is destroyed because of such reentrant transition, consequently the resistance reduces.

Further increasing the magnetic field to $B = 25$ T, the resistivity begins to increase sharply again (Fig. 4a). Since this phenomenon occurs in the ultra-quantum limit where almost all the electrons are confined in the $n = 0$ Landau level, it can be explained as a dynamical mass generation in the $n = 0$ Landau level. The nesting vector of this density wave transition is shown in Fig. 4d. The explicit form of the density wave is inaccessible by the transport experiments, nevertheless, we can theoretically calculate it following ref. 24. With the low-energy Hamiltonian $H_0(\mathbf{k}) = \hbar \left(v_x k_x \tau_x \sigma_z + v_y k_y \tau_y + v_z k_z \tau_x \sigma_x \right) + m\tau_z$, where the Pauli matrices $\tau_{x,y,z}$ refers to certain orbital degrees of freedom and $\sigma_{x,y,z}$ represents the electron spin, and m is a mass parameter that is almost zero. The x, y, z axes correspond to a, c, b axes of the crystal, respectively. Then we have the Landau level wave functions for the zeroth Landau level:

$$\psi_{n=0,\, s=+1,\, k=k_F} = \begin{pmatrix} 0 \\ \cos(\theta_{k_F}/2) \\ \sin(\theta_{k_F}/2) \\ 0 \end{pmatrix} \phi_0, \; \psi_{n=0,\, s=+1,\, k=-k_F}$$

$$= \begin{pmatrix} 0 \\ \cos(\theta_{k_F}/2) \\ -\sin(\theta_{k_F}/2) \\ 0 \end{pmatrix} \phi_0. \tag{3}$$

Here θ_k satisfies $\tan\theta_k = E_k/E_k$, and $E_z = \mu_B g B/2$. Inserting the wave function (3) into the z-component of the spin density $\langle \sigma_z \rangle \propto \exp(2ik_F z - i\alpha_0) \langle \psi_{n=0,\, s=+1,\, k=-k_F} | \sigma_z | \psi_{n=0,\, s=+1,\, k=k_F} \rangle + h.c.$, we have (Supplementary Note 7 and Supplementary Fig. 15)

$$\langle \sigma_z \rangle = m_0 \cos(2k_F z - \alpha_0), \tag{4}$$

where α_0 is a constant phase angle and the constant m_0 can be taken as the order parameter of the density wave. For the first Landau level, the density wave also has the similar form of $\langle \sigma_z \rangle \sim \cos(2k_F z - \alpha_0)$. It would be interesting to demonstrate the

form of density wave state directly in the future experiments such as spin-resolved scanning tunnelling microscopy. And such an exotic field-induced density wave is also confirmed in $HfTe_5$, which has a similar crystal structure and physical properties as $ZrTe_5$ (More details are available in Supplementary Note 8 and Supplementary Figs 16–18).

Discussion

Finally, let us briefly compare $ZrTe_5$ with the previously widely studied Dirac semimetals such as Cd_3As_2. In Cd_3As_2, it is difficult to observe such field-induced density wave transitions with ultra-high magnetic field[49,62] because of their high Fermi velocity along any directions, leading to lower density of states insufficient to achieve pronounced density wave transitions or dynamical mass generation. In contrast, the strong anisotropy of $ZrTe_5$ leads to an exotic layered transport and a quasi-2D Fermi surface. The consequent Fermi velocity along the b axis is very small, which strongly enhances the density of states when the magnetic field is along the b axis. Another advantage of $ZrTe_5$ is the relatively tiny Fermi surface in a–c plane, making it accessible to reach the low Landau level with relatively weak magnetic field. With the strong magnetic field, the electron–electron interaction can be efficiently enhanced, amplifying the instability towards dynamical mass generation. The unambiguous Dirac feature in the a–c plane together with the highly anisotropic Fermi velocity makes $ZrTe_5$ an outstanding platform to study the field-induced instabilities of Dirac fermions.

In summary, we have studied the transport properties of the newly discovered Dirac semimetal $ZrTe_5$, and found signatures of the field-induced dynamical mass generation. As a quasi-2D Dirac material with small Fermi velocity along the layered direction, $ZrTe_5$ is an ideal material to explore field-induced many-body effects. This study may open up a research avenue in the subject of Dirac and Weyl semimetals, namely, field-controlled symmetry-breaking phases manifesting the Dirac mass. In the future, it will also be highly interesting to search for the topological dislocations[35,39,40] of the dynamically generated mass, which may host the dissipationless chiral modes. In a wider perspective, this study shows the possibility of investigating and engineering interaction effects in topological materials, topological semimetals in particular, by applying external fields.

Methods

Sample synthesis and characterizations. High-quality single crystals of $ZrTe_5$ were grown via chemical vapour transport with iodine. Stoichiometric Zirconium flake (99.98%, Alfa Aesar) and Tellurium powder (99.999%, Alfa Aesar) were ground together and sealed in an evacuated quartz tube with iodine flake (99.995%, Alfa Aesar). A temperature gradient of $150\,°C$ between 580 and $430\,°C$ in a two-zone furnace was used for crystal growth. Typical as-grown sample has a long ribbon-like shape. HRTEM was carried out on JEM-2100F. An acceleration voltage of 200 kV was chosen to achieve enough resolution while maintaining the structure of $ZrTe_5$.

Transport measurements. The low-field magneto-transport measurements were performed in a Physical Property Measurement System by Quantum Design with a magnetic up to 9 T. The 60 T pulsed magnetic field measurements were performed at Wuhan National High Magnetic Field Center.

Data availability. The data that support the findings of this study are available from the corresponding author on request.

References

1. DiSalvo, F. J., Fleming, R. M. & Waszczak, J. V. Possible phase transition in the quasi-one-dimensional materials $ZrTe_5$ or $HfTe_5$. *Phys. Rev. B* **24**, 2935–2939 (1981).
2. Okada, S. *et al.* Negative evidences for charge/spin density wave in $ZrTe_5$. *J. Phys. Soc. Jpn* **51**, 460–467 (1982).

3. Whangbo, M., DiSalvo, F. & Fleming, R. Electronic structure of $ZrTe_5$. *Phys. Rev. B* **26**, 687–689 (1982).
4. Kamm, G., Gillespie, D., Ehrlich, A., Wieting, T. & Levy, F. Fermi surface, effective masses, and Dingle temperatures of $ZrTe_5$ as derived from the Shubnikov–de Haas effect. *Phys. Rev. B* **31**, 7617–7623 (1985).
5. Izumi, M. *et al.* Shubnikov-de Haas oscillations and Fermi surfaces in transition-metal pentatellurides $ZrTe_5$ and $HfTe_5$. *J. Phys. C Solid State Phys* **20**, 3691 (1987).
6. Yoshizaki, R., Izumi, M., Harada, S., Uchinokura, K. & Matsuura, E. Shubnikov-de Haas oscillations in transition-metal pentatelluride. *Phys. BC* **117-118**, 605–607 (1983).
7. Weng, H., Dai, X. & Fang, Z. Transition-Metal Pentatelluride $ZrTe_5$ and $HfTe_5$: a Paradigm for Large-Gap Quantum Spin Hall Insulators. *Phys. Rev. X* **4**, 011002 (2014).
8. Li, Q. *et al.* Chiral magnetic effect in $ZrTe_5$. *Nat. Phys.* **12**, 550–554 (2016).
9. Chen, R. Y. *et al.* Magnetoinfrared Spectroscopy of Landau Levels and Zeeman Splitting of Three-Dimensional Massless Dirac Fermions in $ZrTe_5$. *Phys. Rev. Lett.* **115**, 176404 (2015).
10. Chen, R. Y. *et al.* Optical spectroscopy study of the three-dimensional Dirac semimetal $ZrTe_5$. *Phys. Rev. B* **92**, 075107 (2015).
11. Wang, Z. *et al.* Dirac semimetal and topological phase transitions in A_3Bi (A = Na, K, Rb). *Phys. Rev. B* **85**, 195320 (2012).
12. Liu, Z. K. *et al.* Discovery of a three-dimensional topological Dirac semimetal, Na_3Bi. *Science* **343**, 864–867 (2014).
13. Xu, S.-Y. *et al.* Observation of Fermi arc surface states in a topological metal. *Science* **347**, 294–298 (2015).
14. Neupane, M. *et al.* Observation of a three-dimensional topological Dirac semimetal phase in high-mobility Cd_3As_2. *Nat. Commun.* **5**, 3786 (2014).
15. Borisenko, S. *et al.* Experimental realization of a three-dimensional Dirac semimetal. *Phys. Rev. Lett.* **113**, 027603 (2014).
16. Young, S. M. *et al.* Dirac semimetal in three dimensions. *Phys. Rev. Lett.* **108**, 140405 (2012).
17. Ali, M. N. *et al.* Large, non-saturating magnetoresistance in WTe_2. *Nature* **514**, 205–208 (2014).
18. Liang, T. *et al.* Ultrahigh mobility and giant magnetoresistance in the Dirac semimetal Cd_3As_2. *Nat Mater.* **14**, 280–284 (2015).
19. Shekhar, C. *et al.* Extremely large magnetoresistance and ultrahigh mobility in the topological Weyl semimetal candidate NbP. *Nat. Phys.* **11**, 645–649 (2015).
20. Xiong, J. *et al.* Evidence for the chiral anomaly in the Dirac semimetal Na_3Bi. *Science* **350**, 413–416 (2015).
21. Son, D. T. & Spivak, B. Z. Chiral anomaly and classical negative magnetoresistance of Weyl metals. *Phys. Rev. B* **88**, 104412 (2013).
22. Huang, X. *et al.* Observation of the chiral-anomaly-induced negative magnetoresistance in 3D Weyl semimetal TaAs. *Phys. Rev. X* **5**, 031023 (2015).
23. Li, L. *et al.* Phase transitions of Dirac electrons in bismuth. *Science* **321**, 547–550 (2008).
24. Behnia, K., Balicas, L. & Kopelevich, Y. Signatures of electron fractionalization in ultraquantum bismuth. *Science* **317**, 1729–1731 (2007).
25. Fauqué, B. *et al.* Two phase transitions induced by a magnetic field in graphite. *Phys. Rev. Lett.* **110**, 266601 (2013).
26. Fauqué, B., Vignolle, B., Proust, C., Issi, J.-P. & Behnia, K. Electronic instability in bismuth far beyond the quantum limit. *N. J. Phys.* **11**, 113012 (2009).
27. Yang, H. *et al.* Phase diagram of bismuth in the extreme quantum limit. *Nat. Commun.* **1**, 47 (2010).
28. Zhu, Z., Yang, H., Fauqué, B., Kopelevich, Y. & Behnia, K. Nernst effect and dimensionality in the quantum limit. *Nat. Phys.* **6**, 26–29 (2010).
29. Zhu, Z. *et al.* Tunable excitonic insulator in quantum limit graphite. Preprint at http://arxiv.org/abs/1508.03645 (2015).
30. Yang, K.-Y., Lu, Y.-M. & Ran, Y. Quantum Hall effects in a Weyl semimetal: possible application in pyrochlore iridates. *Phys. Rev. B* **84**, 075129 (2011).
31. Sun, X.-Q., Zhang, S.-C. & Wang, Z. Helical spin order from topological Dirac and Weyl semimetals. *Phys. Rev. Lett.* **115**, 076802 (2015).
32. Roy, B. & Sau, J. D. Magnetic catalysis and axionic charge density wave in Weyl semimetals. *Phys. Rev. B* **92**, 125141 (2015).
33. Wei, H., Chao, S.-P. & Aji, V. Excitonic phases from Weyl semimetals. *Phys. Rev. Lett.* **109**, 196403 (2012).
34. Zhang, R.-X. *et al.* Topological nematic phase in Dirac semimetals. *Phys. Rev. B* **93**, 041108 (2016).
35. Wang, Z. & Zhang, S.-C. Chiral anomaly, charge density waves, and axion strings from Weyl semimetals. *Phys. Rev. B* **87**, 161107 (2013).
36. Okada, Y. *et al.* Observation of Dirac node formation and mass acquisition in a topological crystalline insulator. *Science* **341**, 1496–1499 (2013).
37. Zeljkovic, I. *et al.* Dirac mass generation from crystal symmetry breaking on the surfaces of topological crystalline insulators. *Nat. Mater.* **14**, 318–324 (2015).
38. Nambu, Y. & Jona-Lasinio, G. Dynamical model of elementary particles based on an analogy with superconductivity. I. *Phys. Rev.* **122**, 345–358 (1961).
39. Teo, J. C. Y. & Kane, C. L. Topological defects and gapless modes in insulators and superconductors. *Phys. Rev. B* **82**, 115120 (2010).
40. Bi, R. & Wang, Z. Unidirectional transport in electronic and photonic Weyl materials by Dirac mass engineering. *Phys. Rev. B* **92**, 241109 (2015).
41. Lévy, F. & Berger, H. Single crystals of transition metal trichalcogenides. *J. Cryst. Growth* **61**, 61–68 (1983).
42. Manzoni, G. *et al.* Ultrafast optical control of the electronic properties of $ZrTe_5$. *Phys. Rev. Lett.* **115**, 207402 (2015).
43. Qu, D. X., Hor, Y. S., Xiong, J., Cava, R. J. & Ong, N. P. Quantum oscillations and hall anomaly of surface states in the topological insulator Bi_2Te_3. *Science* **329**, 821–824 (2010).
44. Liu, Y. *et al.* Gate-tunable quantum oscillations in ambipolar Cd_3As_2 thin films. *NPG Asia Mater.* **7**, e221 (2015).
45. Schneider, J. M. *et al.* Using magnetotransport to determine the spin splitting in graphite. *Phys. Rev. B* **81**, 195204 (2010).
46. Murakawa, H. *et al.* Detection of Berry's phase in a Bulk Rashba semiconductor. *Science* **342**, 1490–1493 (2013).
47. Shoenberg, D. *Magnetic Oscillations in Metals* (Cambridge Univ. Press, 1984).
48. Li, L. *et al.* Quantum oscillations in a two-dimensional electron gas in black phosphorus thin films. *Nat. Nanotechnol.* **10**, 608–613 (2015).
49. Cao, J. *et al.* Landau level splitting in Cd_3As_2 under high magnetic fields. *Nat. Commun.* **6**, 7779 (2015).
50. Narayanan, A. *et al.* Linear magnetoresistance caused by mobility fluctuations in n-doped Cd_3As_2. *Phys. Rev. Lett.* **114**, 117201 (2015).
51. Yuan, X. *et al.* Observation of quasi-two-dimensional Dirac fermions in $ZrTe_5$. Preprint at http://arxiv.org/abs/1510.00907 (2015).
52. Cao, H. *et al.* Quantized Hall effect and Shubnikov-de haas oscillations in highly doped Bi_2Se_3: evidence for layered transport of bulk carriers. *Phys. Rev. Lett.* **108**, 216803 (2012).
53. Hill, S. *et al.* Bulk quantum Hall effect in η-Mo_4O_{11}. *Phys. Rev. B* **58**, 10778–10783 (1998).
54. Balicas, L., Kriza, G. & Williams, F. I. B. Sign reversal of the quantum Hall number in $(TMTSF)_2(PF)_6$. *Phys. Rev. Lett.* **75**, 2000–2003 (1995).
55. Cooper, J. R. *et al.* Quantized Hall effect and a new field-induced phase transition in the organic superconductor $(TMTSF)_2(PF)_6$. *Phys. Rev. Lett.* **63**, 1984–1987 (1989).
56. Hannahs, S. T., Brooks, J. S., Kang, W., Chiang, L. Y. & Chaikin, P. M. Quantum Hall effect in a bulk crystal. *Phys. Rev. Lett.* **63**, 1988–1991 (1989).
57. Jeon, S. *et al.* Landau quantization and quasiparticle interference in the three-dimensional Dirac semimetal Cd_3As_2. *Nat. Mater.* **13**, 851–856 (2014).
58. Köhler, H. Anisotropic g-factor of the conduction electrons in Bi_2Te_3. *Phys. Status Solidi B* **75**, 127–136 (1976).
59. Yoshioka, D. & Fukuyama, H. Electronic phase transition of graphite in a strong magnetic field. *J. Phys. Soc. Jpn* **50**, 725–726 (1981).
60. Zhang, C. *et al.* Quantum phase transitions in Weyl semimetal tantalum monophosphide. Preprint at http://arxiv.org/abs/1507.06301 (2015).
61. Yaguchi, H. & Singleton, J. Destruction of the field-induced density-wave state in graphite by large magnetic fields. *Phys. Rev. Lett.* **81**, 5193–5196 (1998).
62. Xiang, Z. J. *et al.* Angular-dependent phase factor of Shubnikov-de Haas oscillations in the Dirac semimetal Cd_3As_2. *Phys. Rev. Lett.* **115**, 226401 (2015).

Acknowledgements

Author contributions

F.X. conceived the ideas and supervised the overall research; Y.L. and X.Y. synthetized $ZrTe_5$ single crystals; Y.L., X.Y., C.Z. and J.Z. performed the magnetotransport measurements and analysed the transport data; Zhigang Chen, L.Y., Jin Zou, C.L. and X.W. performed crystal structural analysis; A.N. and S.S. performed the band structure and Fermi surface calculations; Z.W. provided the theoretical calculations and explanations for the magnetotransport; Z.X. and L.L. gave suggestions and guidance of experiments; Y.L. and F.X. wrote the paper with helps from all other co-authors.

Additional information

How to cite this article: Liu, Y. *et al.* Zeeman splitting and dynamical mass generation in Dirac semimetal ZrTe$_5$. *Nat. Commun.* 7:12516 doi: 10.1038/ncomms12516 (2016).